PHOTONICS Research

Multichannel coupling induced topological insulating phases with full multimerization

Jun Li,[1,2,3] Yaping Yang,[1,4] and C.-M. Hu[2,5]

[1]MOE Key Laboratory of Advanced Micro-Structured Materials, School of Physics Science and Engineering, Tongji University, Shanghai 200092, China
[2]Department of Physics and Astronomy, University of Manitoba, Winnipeg, Manitoba R3T 2N2, Canada
[3]e-mail: jli_phys@tongji.edu.cn
[4]e-mail: yang_yaping@tongji.edu.cn
[5]e-mail: hu@physics.umanitoba.ca

Received 18 October 2023; revised 2 January 2024; accepted 9 January 2024; posted 9 January 2024 (Doc. ID 509746); published 1 March 2024

We propose and experimentally realize a class of quasi-one-dimensional topological lattices whose unit cells are constructed by coupled multiple identical resonators, with uniform hopping and inversion symmetry. In the presence of coupling-path-induced effective zero hopping within the unit cells, the systems are characterized by complete multimerization with degenerate −1 energy edge states for open boundary condition. Su–Schrieffer–Heeger subspaces with fully dimerized limits corresponding to pairs of nontrivial flat bands are derived from the Hilbert spaces. In particular, topological bound states in the continuum (BICs) are inherently present in even multimer chains, manifested by embedding the topological bound states into a continuous band assured by bulk-boundary correspondence. Moreover, we experimentally demonstrate the degenerate topological edge states and topological BICs in radio-frequency circuits.

https://doi.org/10.1364/PRJ.509746

1. INTRODUCTION

Topological phases of matter transcend the paradigm of Ginzburg–Landau theory in condensed matter physics, with the absence of any symmetry breaking but derived from geometry, and have attracted extensive investigation in various fields over the past few decades [1–9]. Topological phases are defined by the global wavefunctions of the dispersion bands that pervade the entire system rather than local orbitals, so that they are particularly robust to local perturbations such as defects and impurities. In essence, band structure is the sufficient condition for the existence of topological phases. Since the first discovery of topological phases in quantum electronic systems [1,2], novel and exotic topological properties have been developed in diverse platforms with their own unique advantages such as optics [10,11], acoustics [12,13], mechanics [14], and electric circuits [15–17] in classical regimes and ultra-cold atoms [18,19], trapped ions [20,21], and Fock-state lattices [22,23] in quantum regimes.

One-dimensional (1D) topological phases bring some new insights because of their manipulability and experimental accessibility. The Su–Schrieffer–Heeger (SSH) model of polyacetilene [24,25], as a starting point for 1D topological models based on tight-binding approximation, is a dimerized chain by having two different alternating hopping amplitudes between nearest-neighboring lattice site hosts. Recently, in the context of SSH chains, a variety of extended configurations with new physics and phenomena have been proposed [9,26–30]. On the one hand, special inconsistent inter-site interactions, such as periodically modulated hopping, nonreciprocal hopping, environment-induced coupling, and multi-site coupling, have been introduced to raise a plethora of distinct topological phenomena including but not limited to the non-Hermitian skin effect [31–35], non-Hermitian real spectra [36], dissipative and Floquet topological phase transition [37–40], and trimer topological phases [41–44]. On the other hand, with respect to on-site potentials, the introduction of on-site gain and loss not only provides a pointcut to combine the non-Hermitianity and topological phases for widening topological family [45–47], but also can drive topologically trivial systems and induce topological phase transitions solely by deliberate design [48–52].

Herein, we present a quasi-one-dimensional (quasi-1D) tight-binding configuration without any staggered hopping and on-site potentials. We consider unit cells of multiple identical resonators with uniform coupling between every two sites and the same strength as the inter-cell coupling, i.e., only one kind of coupling strength and resonators in the whole chain. The system then forms complete multimer due to the zero effective intracell hopping induced by special coupling paths. Conceivably, considering the bulk-boundary correspondence (BBC), degenerate topological edge states with full localization exist in finite systems. Interestingly, with the increase of

resonators in the unit cell, pairs of nontrivial flat bands appear at two fixed frequencies, which correspond to fully dimerized subspaces derived from the Hilbert spaces. Moreover, for even multimer chains, topological bound states in the continuum (BICs) [53] naturally form via the bandgap of nontrivial flat bands just covered by a trivial band. We experimentally implement the idea by using AC circuits consisting of uniform capacitors and inductors.

2. THEORETICAL MODELS AND EDGE STATES

We start by considering a tight-binding system consisting of n ($n \geq 3$) identical resonators coupled to each other with the same hopping amplitude κ, as shown in Fig. 1(a). Here, we consider a Hermitian system in which the intrinsic and coupling losses of all the resonators are ignored and κ is sufficiently small compared to the frequency of resonators ω_0. The systems can be represented by the Hamiltonian

$$H_n = \begin{pmatrix} 0 & \kappa & \kappa & \cdots \\ \kappa & 0 & \kappa & \cdots \\ \kappa & \kappa & 0 & \cdots \\ \vdots & \vdots & \vdots & \ddots \end{pmatrix}_{n\times n}, \quad (1)$$

characterized by the diagonal elements of the matrix being zero and all the others being κ. Interestingly, there are always degenerate states with a fixed frequency independent of n in the system. Specifically, with reference to ω_0, one of its eigenvalues is $\lambda_n = (n-1)\kappa$ with the normalized eigenvectors $|\psi_n\rangle = (1/\sqrt{n}, 1/\sqrt{n}, \ldots, 1/\sqrt{n})'$ while the others are $\lambda_i = -\kappa$ where $i = 1, 2, \ldots, n-1$ with the corresponding eigenvectors $|\psi_i\rangle = (0, \ldots, 0, 1/\sqrt{2})'$ where the ith element $|\psi_i\rangle_i = 1/\sqrt{2}$.

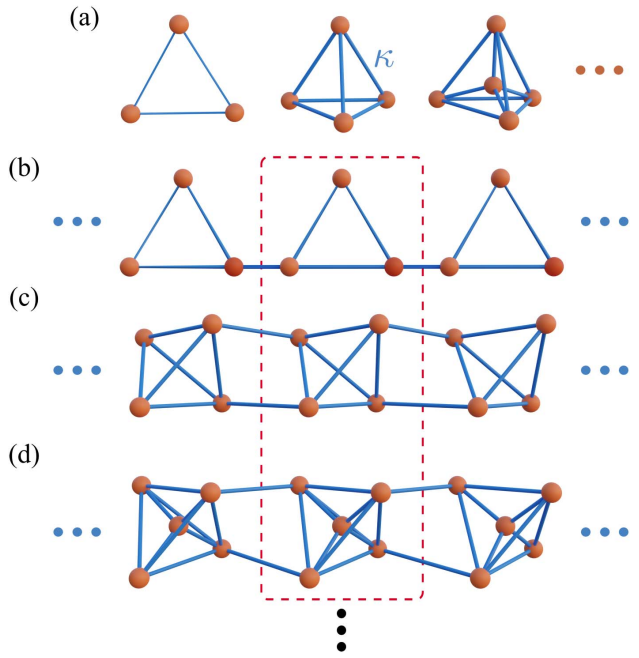

Fig. 1. Theoretical tight-binding hopping model. (a) Schematic of n ($n = 3, 4, 5\ldots$) resonators coupled with each other with uniform hopping amplitude κ. (b)–(d) Bulk model with n sites per unit cell, with uniform hoppings, unit cells framed in red dashed box.

In terms of the splitting of eigenvalues, the local effective coupling between the degenerate modes can be seen as zero to some extent.

With this supposition, as shown in Figs. 1(b)–1(d), we design a class of quasi-1D lattices with the above coupling multiple resonators as their unit cell. The unit cells are coupled to their nearest neighbor through $[n/2]$ independent coupling channels with the same hopping amplitudes κ. Considering the zero effective intracell hopping, we can expect that our chains are topologically nontrivial with complete multimerization. In bulk momentum space, the Bloch Hamiltonian of the chain can be written as

$$H_n(k) = \begin{pmatrix} 0 & \kappa & \cdots & \kappa + \kappa e^{-ika} \\ \kappa & 0 & \cdots & \kappa \\ \vdots & \vdots & \ddots & \vdots \\ \kappa + \kappa e^{ika} & \kappa & \cdots & 0 \end{pmatrix}_{n\times n}, \quad (2)$$

where a is the lattice constant between the units and k is the Bloch wave number. The Bloch Hamiltonian shows that the Bloch term $\kappa e^{\pm ika}$ only exists in all anti-diagonal elements, provided that the diagonal term remains zero. The multichannel inter-cell coupling term κ appears in all elements of the matrix except the diagonal entries. Obviously, the Hamiltonian displays inversion ($\mathcal{I}$) symmetry, i.e., $\mathcal{I}H_n(k)\mathcal{I}^{-1} = H_n(-k)$. For clarity, the system is classified into two patterns via n that is odd or even in the following analysis. We find the analytical solutions of its energy spectra expressed as

$$\omega_{n,o}(k) = \begin{pmatrix} -2 \\ \vdots \\ n/3 - 1 - (A_+ + i\sqrt{3}A_-)/2 \\ n/3 - 1 - (A_+ - i\sqrt{3}A_-)/2 \\ 0 \\ \vdots \\ n/3 - 1 + A_+ \end{pmatrix} \kappa, \quad (3)$$

when n is odd where $A_\pm = C/B \pm B$, $B = (\sqrt{D^2 - C^3} + D)^{1/3}$, $C = (n-1)\cos ka/3 + (n^2+3)/9$, and $D = (n^2 - n)\cos ka/6 + (n/3)^3 + (n-3)/6$. Surprisingly, there are $n-3$ flat bands equally divided at $\omega_n = 0$ and $\omega_n = -2\kappa$. And only two bandgaps with the width $G_1 = \sqrt{(n-2)^2+1} - \sqrt{(n-1)^2-1} + 1$ and $G_2 = \sqrt{(n-2)^2+1} + n - 2$ exist in the energy spectra. For the case where n is even, the eigenfrequency is given by

$$\omega_{n,e}(k) = \begin{pmatrix} -2 \\ \vdots \\ n/2 - 1 - \sqrt{n^2/4 + 1 + n\cos ka} \\ 0 \\ \vdots \\ n/2 - 1 + \sqrt{(n^2/4 + 1 + n\cos ka} \end{pmatrix} \kappa, \quad (4)$$

characterized by having $n/2-1$ flat bands at $\omega_n = 0$ and $\omega_n = -2\kappa$, respectively. The $(n/2)$th band and the top (nth)

band are symmetric with respect to $(n/2-1)\kappa$. It is noteworthy that as the parameter n varies, there consistently exists one bandgap with a width of $G = n-2$ due to the lower nonflat band precisely overlapping the bandgap of the flat bands. In both cases, the band structure of the bulk Hamiltonian is not symmetric around zero, indicating that our chain is chiral symmetry broken. In detail, except for the top band that exceeds zero, the other bands are always distributed between -2κ and zero.

Figures 2(a)–2(c) show the band structures in first Brillouin zone for different n. Here, in the presence of inversion symmetry, we introduce the Zak phase, defined as $Z_j = -i\int_{-\pi/a}^{\pi/a}\langle\psi_{k,j}|\partial_k|\psi_{k,j}\rangle \mathrm{d}k$, to characterize the topology of our 1D multimer system where j specifies the occupied band index with corresponding Bloch wavefunctions $|\psi_{k,j}\rangle$ [54]. We can obtain nonzero quantized Zak phases of bands for various n, indicating the topological nontriviality of our chains. Particularly, the top band possesses a Zak phase of zero while the flat bands always have Zak phases of $-\pi$. We can block-diagonalize $H_n(k)$ by unitary transformation $\mathcal{U}_n^{-1}H_n(k)\mathcal{U}_n = H_n^{BD}(k)$ to show the separation between flat and nonflat bands clearly. For the simplest case with $n = 4$, the unitary matrix and the block-diagonal Hamiltonian are

$$\mathcal{U}_4 = \frac{1}{\sqrt{2}}\begin{pmatrix} 1 & 0 & 1 & 0 \\ 1 & 0 & -1 & 0 \\ 0 & 1 & 0 & -1 \\ 0 & 1 & 0 & 1 \end{pmatrix}, \tag{5}$$

$$H_4^{\mathrm{BD}}(k) = \begin{pmatrix} 1 & 2+e^{-ika} & 0 & 0 \\ 2+e^{ika} & 1 & 0 & 0 \\ 0 & 0 & -1 & e^{-ika} \\ 0 & 0 & e^{ika} & -1 \end{pmatrix}\kappa, \tag{6}$$

respectively. As expected, the 2×2 blocks have the same form as the SSH Hamiltonian where the upper one is topologically trivial corresponding to the blue bands and the lower block is topologically nontrivial with complete dimerization corresponding to the flat bands. More generally, the bulk Hamiltonians for larger n can be divided into a topological trivial dimerized subspace and $n/2-1$ nontrivial fully dimerized subspaces by the unitary transformation when n is even. Moreover, the lower trivial band for the even chain always spans the bandgap between the flat bands by meeting the upper and lower flat bands at the boundary and center of the first Brillouin zone, respectively. Similarly, for odd n, we can get the block-diagonal Hamiltonian composed of a 3×3 block and $(n-3)/2$ same nontrivial 2×2 blocks (see Appendix C for details) where the 3×3 subspace owns two nontrivial lower bands in contact with the upper and lower flat bands independently.

Considering the BBC, under the open boundary condition, we show the normalized eigenvalue spectra ω_i/κ of finite multimer chains with 60 resonators in Figs. 2(d)–2(f) and the corresponding wavefunctions $|\psi_i\rangle$ in Figs. 2(g)–2(i) for $n = 3$, 4, and 5. Mathematically, the wavefunction solution is not unique for the finite-size chains with $n > 3$, owing to the fact that the rank of the Hamiltonian matrix is smaller than the matrix

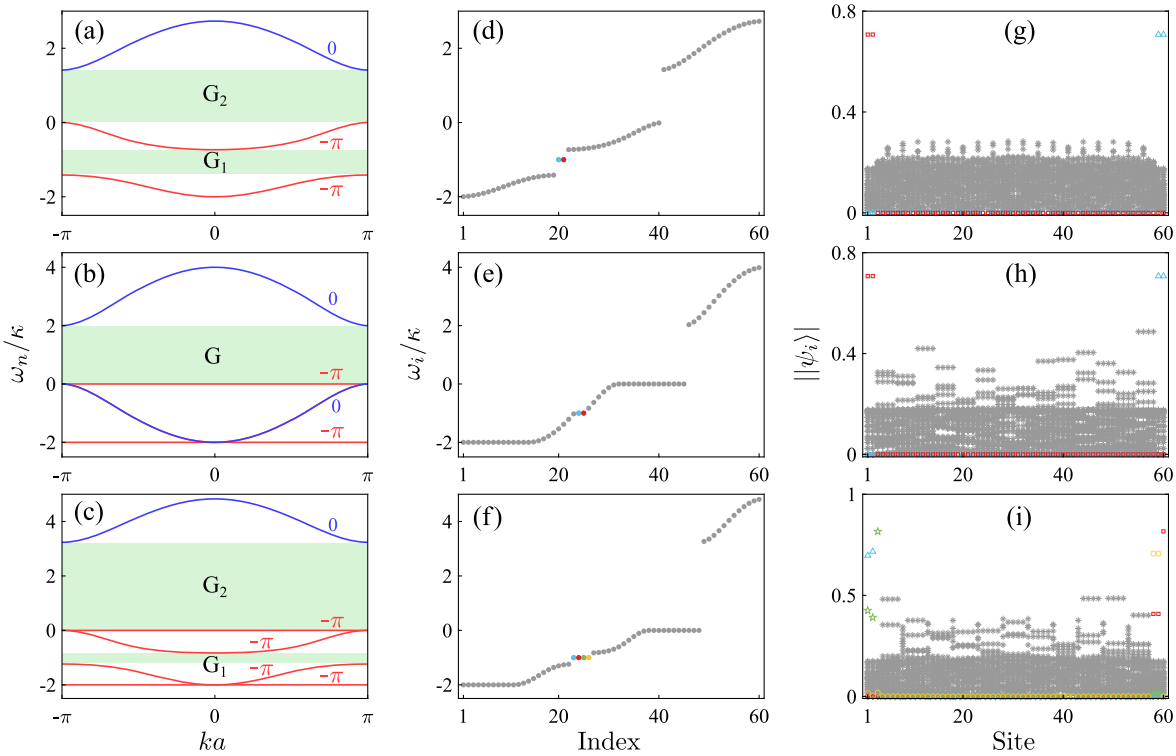

Fig. 2. Topological edge states of multimer chains. (a)–(c) Normalized band structures with quantized Zak phases and (d)–(f) sorted eigenvalues of topological finite chains (composed of 60 resonators) with (g)–(i) corresponding representative wavefunctions for (a), (d), (g) $n = 3$; (b), (e), (h) $n = 4$; and (c), (f), (i) $n = 5$, respectively. Zak phases for the bands labeled by red are $-\pi$ and 0 by blue in (a)–(c). The edge and bulk states in (d)–(f) with the corresponding intensity distributions in (g)–(i) are represented by color and gray, respectively. Particularly, the wavefunction distributions in panels (h) and (i) represent individual instances of potential numerical solutions for $n = 4$ and $n = 5$, respectively.

dimension. The wavefunction distributions depicted in Figs. 2(h) and 2(i) exemplify potential numerical solutions for $n = 4$ and $n = 5$, respectively. Correspondingly, there are pairs of degenerate edge states marked by the colored dots at the exact detuning $-\kappa$ with the same number as the nontrivial bands. The topological edge modes of the odd multimer chain sit in the lower bandgap G_1. Remarkably, the topological edge states are clearly embedded in the continuous spectrum of the lower nontrival band and are the so-called topological BICs [53] when n is even. Because of the complete multimerization, the wavefunctions of exact −1 energy edge modes are absolutely localized at the two boundary cells without any distribution in the bulk, while the bulk wavefunctions are diffused throughout the whole chains. Therefore, the edge states are also completely robust to the local perturbations of frequency and coupling strength of bulk resonators.

3. EXPERIMENTAL OBSERVATIONS

We employ periodic radio-frequency inductor-capacitor (LC) circuits featuring flexible hopping channels to experimentally observe the tight-binding modes. Here, the lattice nodes are capacitively coupled to ground and inductively coupled to each other. The multimer chains can be represented by the admittance matrix J_ω (also termed circuit Laplacian) [17,47,55]. The voltage response $\boldsymbol{V}(\omega)$ of the nodes to an input current $\boldsymbol{I}(\omega)$ at frequency ω follows Kirchhoff's law: $\boldsymbol{I}(\omega) = J(\omega)\boldsymbol{V}(\omega)$, where the vectors $\boldsymbol{I}(\omega) = [I_1, I_2, \ldots, I_s]'$ and $\boldsymbol{V}(\omega) = [V_1, V_2, \ldots, V_s]'$ for s nodes circuit. For our uniform hopping chains, using the same size capacitors C and inductors L, we have the circuit Laplacian

$$J(\omega) = \frac{1}{i\omega}\left[\left(\frac{n}{L} - \omega^2 C\right)\mathbb{I} + H\right] \tag{7}$$

with

$$H = \begin{pmatrix} 0 & -1/L & -1/L & \cdots \\ -1/L & 0 & -1/L & \cdots \\ -1/L & -1/L & 0 & \cdots \\ \vdots & \vdots & \vdots & \ddots \end{pmatrix}_{s\times s}, \tag{8}$$

where $\mathbb{I}$ is the $s \times s$ unit matrix and H can represent our theoretical model accurately with the hopping amplitude $-1/L$. We construct periodic LC circuits with 24 nodes for trimer and tetramer configurations as shown in Figs. 3(a) and 4(a), respectively. By solving the eigenvalues E_i of H numerically, we can obtain the general admittance eigenspectral dispersion as $f_i = \sqrt{(n/L + E_i)/C}/(2\pi)$ with degenerate edge states labeled by red shown in Figs. 3(b) and 4(b). It is obvious that the edge states shown in Fig. 4(b) are located in the middle of the continuous energy band for the tetrameric circuit. Note that the inverted nonlinear spectra are due to the negative frequency-dependent hopping amplitude of inductive coupling.

In the experiment implementation, we choose the circuit components: $C = 1$ nF with ±1% tolerance and $L = 1.1$ μH with ±5% deviation. Details of the sample fabrication and impedance measurements are provided in the Appendix A. Measured impedances of nodes 1, 13, and 17 to ground ($|Z_1|$, $|Z_{13}|$, and $|Z_{17}|$) versus the frequency of input circuit

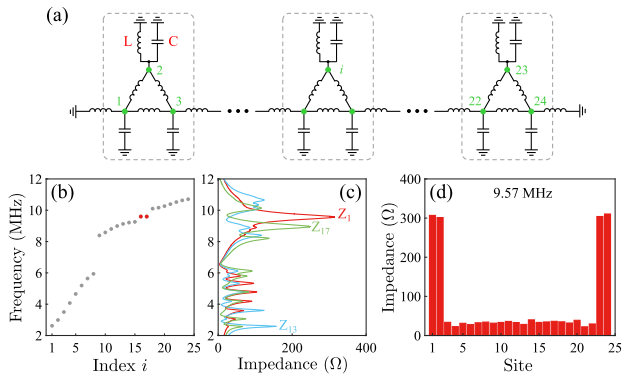

Fig. 3. Observation of topological edge states in trimer chain. (a) Circuit diagram of the finite experimental trimer chain; unit cells consist of three capacitors C with identical inductors L between every two capacitors framed in gray dashed boxes. The lattice nodes are marked by the green dots. (b) Calculated admittance eigenspectrum of the LC circuit for $C = 1$ nF and $L = 1.1$ μH. (c) Measured impedances between the nodes ($|Z_1|$, $|Z_{13}|$, and $|Z_{17}|$) and ground versus the frequency of the circuit. (d) Location distribution of impedance at the frequency $f = 9.57$ MHz.

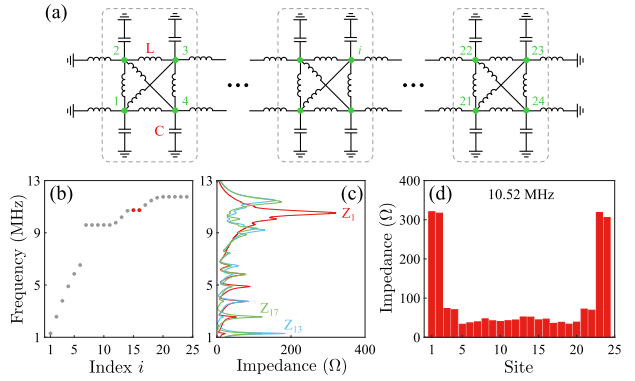

Fig. 4. Observation of topological BICs in tetramer chain. (a) Circuit diagram blueprint with unit cells framed in gray dashed boxes and nodes marked by green dots. (b) Calculated admittance eigenvalues of the tetramer LC circuit for $C = 1$ nF and $L = 1.1$ μH. (c) Frequency scan of measured impedances for representative edge ($|Z_1|$) and bulk ($|Z_{13}|$ and $|Z_{17}|$) nodes. (d) Impedance distribution of topological edge mode at the frequency $f = 10.52$ MHz.

are shown in Figs. 3(c) and 4(c) for trimer and tetramer chain, respectively. The peak frequencies of the impedances are in good agreement with the calculated eigenvalues, despite some slight frequency shift of the measured impedance peaks due to component tolerances. In Fig. 3(c), the highest impedance peak near 9.57 MHz of the edge node inside the band gap (about 9.25–10.1 MHz) with impedance valleys for bulk nodes denotes the topological modes unambiguously. More intuitively, we measure the impedance distribution of the degenerate topological edge modes with strong locality at both ends at 9.57 MHz shown in Fig. 3(d). Differently, corresponding to the calculated eigenspectrum, the impedance peak of the edge node is accompanied by the impedance peaks of the bulk nodes near the frequency of edge state 10.52 MHz in Fig. 4(c),

representing the existence of a topological bound state in a nontopological continuum where the bound edge states are shown in Fig. 4(d).

4. CONCLUSION

In summary, we theoretically and experimentally demonstrated degenerate topological edge states in a class of topological multimer chains consisting of identical resonators with uniform hopping. By designing deliberate coupling paths, the systems exhibit full multimerization with fully dimerized SSH subspaces corresponding to flat bands that can be separated from their Hilbert spaces. We also show topological BICs by embedding the degenerate topological bound states into a continuous band in even chains naturally. These phenomena indicate some potential applications in various fields. Our scheme is experimentally accessible and can also be implemented in coupled waveguide arrays [56], optical and acoustic coupled cavity arrays [53,57], cold atom lattices [58], and three-dimensional circuit quantum electrodynamics [59]. Our work sheds new light on the construction of topological phases.

APPENDIX A: EXPERIMENTAL SETUP

For our experimental setup, we fabricate the topological chains on printed circuit boards (PCBs) with 24 nodes as shown in Fig. 5. The circuit elements are all surface-mount devices (SMDs) with a uniform Electronic Industries Alliance (EIA) size 0603, i.e., 1206 for metric size. Specifically, we choose surface mount multilayer ceramic chip capacitors (SMD MLCCs) with the mean value of 1 nF and the tolerance of ±1% and multilayer ferrite (MLF) inductors with the mean value of 1.1 μH and the tolerance of ±5%. Moreover, the thick film chip resistors with the mean value of 0.1 Ω and the tolerance of ±1% are introduced in series with the capacitors as perturbations. The on-site resistors can mask frequency fluctuations caused by capacitance and inductance tolerances to a certain extent, because they reduce the quality value of the circuit resonator but do not change its frequency [55].

As shown in Fig. 6, we indirectly measure the impedances of the nodes to ground using the vector network analyzer (VNA) Keysight E5080B 9 kHz–20 GHz. For single-port load impedance Z, the reflection coefficient S_{11} is given as [60]

$$S_{11} = \frac{Z - R_0}{Z + R_0}, \tag{A1}$$

where $R_0 = 50\ \Omega$ is the terminal impedance of VNA port (Port 1). By measuring the S-parameter S_{11} of the node, the node impedance can be obtained by [60]

$$Z = \frac{1 + S_{11}}{1 - S_{11}} R_0. \tag{A2}$$

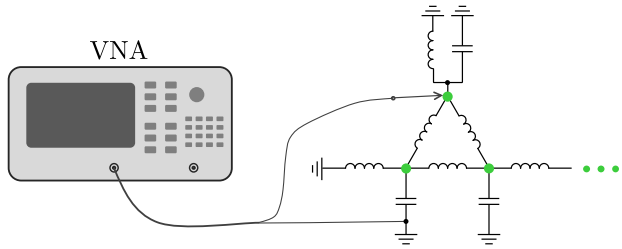

Fig. 6. Schematic diagram of the experimental measurement setup where the green dots indicate wiring for measuring.

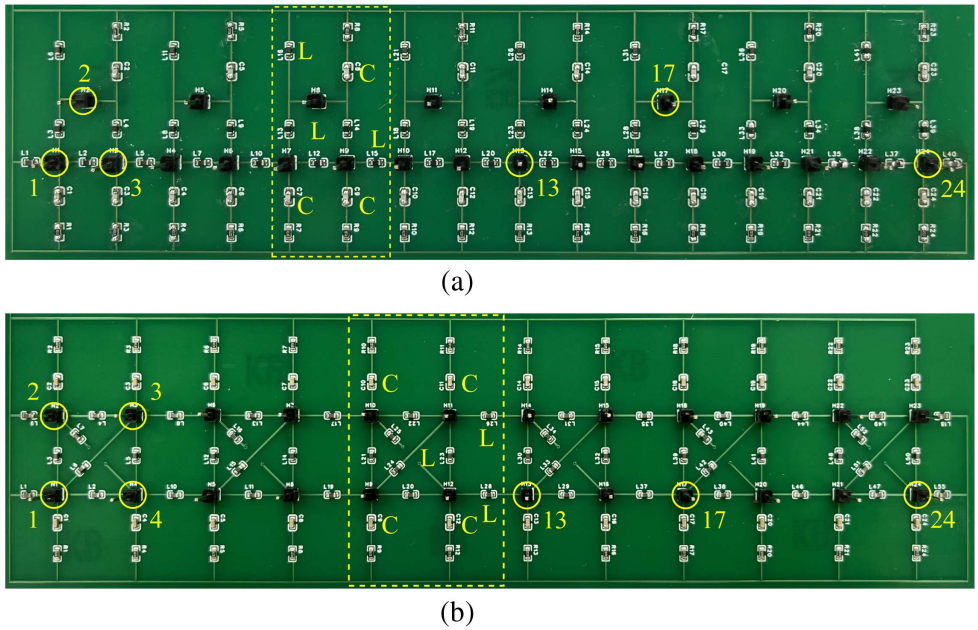

Fig. 5. Photograph of circuit boards realization for (a) trimer chain and (b) tetramer chain. Unit cells of the boards are framed in the dashed boxes. The single pin header connectors at wire junctions are the nodes of circuits. The nodes are labeled by site 1 to 24 from left to right as circled. Inductors L between the nodes realize the hoppings and inductors to ground are to ensure a uniform frequency. Capacitors C connect each node to ground.

APPENDIX B: ADMITTANCE FORMALISM

For the basic linear components of electric circuits—resistors, capacitors, and inductors—the current I flowing through them versus their loading voltage V is given by

$$I = \frac{1}{R}V, \quad I = C\frac{\mathrm{d}V}{\mathrm{d}t}, \quad \frac{\mathrm{d}I}{\mathrm{d}t} = \frac{1}{L}V, \tag{B1}$$

respectively, where R is the resistance of the resistor element, C is the capacitance of the capacitor, and L is the inductance of the inductor. Considering the harmonic circuit with the frequency ω, for $I = I_0 e^{-i\omega t}$ and $V = V_0 e^{-i\omega t}$, their effective impedances can be expressed as

$$Z_R(\omega) = R, \quad Z_C(\omega) = \frac{1}{-i\omega C}, \quad Z_L(\omega) = -i\omega L. \tag{B2}$$

Following Kirchhoff's nodal law, in the frequency domain, the external input current $I_j(\omega)$ into each node is equal to the sum of currents flowing to their nearest neighbor nodes and ground. For our periodic circuit composed of uniform capacitors and inductors with inductive coupling, ignoring the on-site resistors, we can get the linear equation of each node:

$$I_j(\omega) = I_{j0} + \sum_{k=1}^{n} I_{jk} = \frac{V_j(\omega)}{Z_C(\omega)} + \sum_{k=1}^{n} \frac{V_j(\omega) - V_k(\omega)}{Z_L(\omega)}, \tag{B3}$$

where k is the index of nodes or ground connected to the node j by inductors and n is the number of nodes within a unit cell. Integrating the relations between the input current $I_j(\omega)$ of each node and their node voltage $V_j(\omega)$, the matrix equation emerges as follows:

$$\boldsymbol{I}(\omega) = J(\omega)\boldsymbol{V}(\omega), \tag{B4}$$

where the vectors $\boldsymbol{I}(\omega) = [I_1, I_2, \ldots, I_{24}]'$ and $V(\omega) = [V_1, V_2, \ldots, V_{24}]'$ for our 24 nodes circuit and the admittance matrix $J(\omega)$ is

$$J(\omega) = \frac{1}{i\omega}\left[\left(\frac{n}{L} - \omega^2 C\right)\mathbb{I} + H\right]. \tag{B5}$$

where $\mathbb{I}$ is the 24×24 unit matrix and the matrix

$$H = \begin{pmatrix} 0 & -1/L & -1/L & 0 & 0 & 0 & \cdots \\ -1/L & 0 & -1/L & 0 & 0 & 0 & \cdots \\ -1/L & -1/L & 0 & -1/L & 0 & 0 & \cdots \\ 0 & 0 & -1/L & 0 & -1/L & -1/L & \cdots \\ 0 & 0 & 0 & -1/L & 0 & -1/L & \cdots \\ 0 & 0 & 0 & -1/L & -1/L & 0 & \cdots \\ \vdots & \vdots & \vdots & \vdots & \vdots & \vdots & \ddots \end{pmatrix}_{24\times 24}, \tag{B6}$$

for trimer chain ($n = 3$);

$$H = \begin{pmatrix} 0 & -1/L & -1/L & -1/L & 0 & 0 & 0 & 0 & \cdots \\ -1/L & 0 & -1/L & -1/L & 0 & 0 & 0 & 0 & \cdots \\ -1/L & -1/L & 0 & -1/L & 0 & -1/L & 0 & 0 & \cdots \\ -1/L & -1/L & -1/L & 0 & -1/L & 0 & 0 & 0 & \cdots \\ 0 & 0 & 0 & -1/L & 0 & -1/L & -1/L & -1/L & \cdots \\ 0 & 0 & -1/L & 0 & -1/L & 0 & -1/L & -1/L & \cdots \\ 0 & 0 & 0 & 0 & -1/L & -1/L & 0 & -1/L & \cdots \\ 0 & 0 & 0 & 0 & -1/L & -1/L & -1/L & 0 & \cdots \\ \vdots & \vdots & \vdots & \vdots & \vdots & \vdots & \vdots & \vdots & \ddots \end{pmatrix}_{24\times 24}, \tag{B7}$$

when $n = 4$, i.e., for the tetramer circuit.

APPENDIX C: SUBSPACE DECOMPOSITION

As stated in the main text, the flat and nonflat bands can be separated by unitary transformation. For the simplest case of odd multimer chain with flat bands ($n = 5$), the unitary matrix is

$$\mathcal{U}_5 = \frac{1}{\sqrt{2}}\begin{pmatrix} 1/\sqrt{2} & 0 & 1/\sqrt{2} & 0 & 1 \\ 1/\sqrt{2} & 0 & 1/\sqrt{2} & 0 & -1 \\ 1 & 0 & -1 & 0 & 0 \\ 0 & 1 & 0 & 1 & 0 \\ 0 & 1 & 0 & -1 & 0 \end{pmatrix}, \tag{C1}$$

and the corresponding two divided subspaces Hamiltonians are

$$H_{3\times 3} = \begin{pmatrix} 1/2 + \sqrt{2} & \sqrt{2} + 1 + K_+ & 1/2 \\ \sqrt{2} + 1 + K_- & 1 & \sqrt{2} - 1 + K_- \\ 1/2 & \sqrt{2} - 1 + K_+ & 1/2 - \sqrt{2} \end{pmatrix}\kappa \tag{C2}$$

and

$$H_{2\times 2} = \begin{pmatrix} -1 & e^{-ika} \\ e^{ika} & -1 \end{pmatrix}\kappa. \tag{C3}$$

where $K_\pm = \sqrt{2}e^{\pm ika}/2$. The upper 3×3 block corresponding to the three nonflat bands is topologically nontrival with

one zero-Zak-phase top band and two $-\pi$-Zak-phase lower bands while the 2×2 subspace is nontrivial SSH Hamiltonian with fully dimerized limits. With the increase of Hilbert spaces, the bulk Hamiltonians of odd multimer chains can be divided into a 3×3 Hamiltonian H_{o1} and $(n-3)/2$ same nontrivial 2×2 blocks H_{o2} where

$$H_{o1}=\begin{pmatrix} X_+ & Y_++K_+ & (n-3)/4 \\ Y_++K_- & (n-3)/2 & Y_-+K_- \\ (n-3)/4 & Y_-+K_+ & X_- \end{pmatrix}\kappa, \tag{C4}$$

$$H_{o2}=\begin{pmatrix} -1 & e^{-ika} \\ e^{ika} & -1 \end{pmatrix}\kappa, \tag{C5}$$

where $X_\pm=(n-3)/4\pm\sqrt{(n-1)/2}$ and $Y_\pm=\sqrt{2}(n-1)/4\pm\sqrt{(n-1)}/2$. The corresponding unitary matrix is too lengthy to be given. And for even n, the Hilbert spaces can be block-diagonalized into a topological trivial dimerized subspace H_{e1} and $n/2-1$ nontrivial fully dimerized subspaces H_{e2} where

$$H_{e1}=\begin{pmatrix} n/2-1 & n/2+e^{-ika} \\ n/2+e^{ika} & n/2-1 \end{pmatrix}\kappa, \tag{C6}$$

$$H_{e2}=\begin{pmatrix} -1 & e^{-ika} \\ e^{ika} & -1 \end{pmatrix}\kappa. \tag{C7}$$

Both H_{o2} and H_{e2} have the same format as a nontrivial SSH Hamiltonian with full dimerization, corresponding to the flat bands.

Funding. National Natural Science Foundation of China (12274326); National Key Research and Development Program of China (2021YFA1400600, 2021YFA1400602); China Scholarship Council (202106260079).

Acknowledgment. C.-M. Hu acknowledgments support from NSERC Discovery Grants and NSERC Discovery Accelerator Supplements.

Disclosures. The authors declare no conflicts of interest.

Data Availability. Data underlying the results presented in this paper are not publicly available at this time but may be obtained from the authors upon reasonable request.

REFERENCES

1. K. V. Klitzing, G. Dorda, and M. Pepper, "New method for high-accuracy determination of the fine-structure constant based on quantized hall resistance," Phys. Rev. Lett. **45**, 494–497 (1980).
2. D. J. Thouless, M. Kohmoto, M. P. Nightingale, *et al.*, "Quantized Hall conductance in a two-dimensional periodic potential," Phys. Rev. Lett. **49**, 405–408 (1982).
3. F. D. M. Haldane, "Model for a quantum Hall effect without landau levels: condensed-matter realization of the "parity anomaly"," Phys. Rev. Lett. **61**, 2015–2018 (1988).
4. M. Z. Hasan and C. L. Kane, "Colloquium: topological insulators," Rev. Mod. Phys. **82**, 3045–3067 (2010).
5. X.-L. Qi and S.-C. Zhang, "Topological insulators and superconductors," Rev. Mod. Phys. **83**, 1057–1110 (2011).
6. A. Bansil, H. Lin, and T. Das, "Colloquium: topological band theory," Rev. Mod. Phys. **88**, 021004 (2016).
7. C.-K. Chiu, J. C. Y. Teo, A. P. Schnyder, *et al.*, "Classification of topological quantum matter with symmetries," Rev. Mod. Phys. **88**, 035005 (2016).
8. X.-G. Wen, "Colloquium: zoo of quantum-topological phases of matter," Rev. Mod. Phys. **89**, 041004 (2017).
9. E. J. Bergholtz, J. C. Budich, and F. K. Kunst, "Exceptional topology of non-Hermitian systems," Rev. Mod. Phys. **93**, 015005 (2021).
10. L. Lu, J. D. Joannopoulos, and M. Soljačić, "Topological photonics," Nat. Photonics **8**, 821–829 (2014).
11. T. Ozawa, H. M. Price, A. Amo, *et al.*, "Topological photonics," Rev. Mod. Phys. **91**, 015006 (2019).
12. Z. Yang, F. Gao, X. Shi, *et al.*, "Topological acoustics," Phys. Rev. Lett. **114**, 114301 (2015).
13. M. Xiao, G. Ma, Z. Yang, *et al.*, "Geometric phase and band inversion in periodic acoustic systems," Nat. Phys. **11**, 240–244 (2015).
14. S. D. Huber, "Topological mechanics," Nat. Phys. **12**, 621–623 (2016).
15. V. V. Albert, L. I. Glazman, and L. Jiang, "Topological properties of linear circuit lattices," Phys. Rev. Lett. **114**, 173902 (2015).
16. N. Jia, C. Owens, A. Sommer, *et al.*, "Time- and site-resolved dynamics in a topological circuit," Phys. Rev. X **5**, 021031 (2015).
17. C. H. Lee, S. Imhof, C. Berger, *et al.*, "Topolectrical circuits," Commun. Phys. **1**, 39 (2018).
18. N. R. Cooper, J. Dalibard, and I. B. Spielman, "Topological bands for ultracold atoms," Rev. Mod. Phys. **91**, 015005 (2019).
19. J. Perczel, J. Borregaard, D. E. Chang, *et al.*, "Topological quantum optics in two-dimensional atomic arrays," Phys. Rev. Lett. **119**, 023603 (2017).
20. N. Hao and J. Hu, "Topological quantum states of matter in iron-based superconductors: from concept to material realization," Natl. Sci. Rev. **6**, 213–226 (2018).
21. P. T. Dumitrescu, J. G. Bohnet, J. P. Gaebler, *et al.*, "Dynamical topological phase realized in a trapped-ion quantum simulator," Nature **607**, 463–467 (2022).
22. H. Cai and D.-W. Wang, "Topological phases of quantized light," Natl. Sci. Rev. **8**, nwaa196 (2020).
23. J. Deng, H. Dong, C. Zhang, *et al.*, "Observing the quantum topology of light," Science **378**, 966–971 (2022).
24. W. P. Su, J. R. Schrieffer, and A. J. Heeger, "Solitons in polyacetylene," Phys. Rev. Lett. **42**, 1698–1701 (1979).
25. A. J. Heeger, S. Kivelson, J. R. Schrieffer, *et al.*, "Solitons in conducting polymers," Rev. Mod. Phys. **60**, 781–850 (1988).
26. K. Kawabata, K. Shiozaki, M. Ueda, *et al.*, "Symmetry and topology in non-Hermitian physics," Phys. Rev. X **9**, 041015 (2019).
27. G. Li, L. Wang, R. Ye, *et al.*, "Direct extraction of topological ZAK phase with the synthetic dimension," Light Sci. Appl. **12**, 81 (2023).
28. Y. Li, Y. Wang, H. Zhao, *et al.*, "Interaction-induced breakdown of chiral dynamics in the Su-Schrieffer-Heeger model," Phys. Rev. Res. **5**, L032035 (2023).
29. Q. Yuan, L. Gu, L. Fang, *et al.*, "Giant enhancement of nonlinear harmonic generation in a silicon topological photonic crystal nanocavity chain," Laser Photonics Rev. **16**, 2100269 (2022).
30. V. Gupta and B. Bradlyn, "Wannier-function methods for topological modes in one-dimensional photonic crystals," Phys. Rev. A **105**, 053521 (2022).
31. T. E. Lee, "Anomalous edge state in a non-Hermitian lattice," Phys. Rev. Lett. **116**, 133903 (2016).
32. S. Yao and Z. Wang, "Edge states and topological invariants of non-Hermitian systems," Phys. Rev. Lett. **121**, 086803 (2018).
33. F. Song, S. Yao, and Z. Wang, "Non-Hermitian topological invariants in real space," Phys. Rev. Lett. **123**, 246801 (2019).
34. N. Okuma, K. Kawabata, K. Shiozaki, *et al.*, "Topological origin of non-Hermitian skin effects," Phys. Rev. Lett. **124**, 086801 (2020).
35. T. Helbig, T. Hofmann, S. Imhof, *et al.*, "Generalized bulk–boundary correspondence in non-Hermitian topolectrical circuits," Nat. Phys. **16**, 747–750 (2020).
36. Y. Long, H. Xue, and B. Zhang, "Non-hermitian topological systems with eigenvalues that are always real," Phys. Rev. B **105**, L100102 (2022).

37. W. Nie, M. Antezza, Y.-X. Liu, *et al.*, "Dissipative topological phase transition with strong system-environment coupling," Phys. Rev. Lett. **127**, 250402 (2021).
38. C. Fan, X. Shi, F. Wu, *et al.*, "Photonic topological transition in dimerized chains with the joint modulation of near-field and far-field couplings," Photonics Res. **10**, 41–49 (2022).
39. M. Jangjan, L. E. F. Foa Torres, and M. V. Hosseini, "Floquet topological phase transitions in a periodically quenched dimer," Phys. Rev. B **106**, 224306 (2022).
40. J. M. P. Nair, M. O. Scully, and G. S. Agarwal, "Topological transitions in dissipatively coupled Su-Schrieffer-Heeger models," Phys. Rev. B **108**, 184304 (2023).
41. W. P. Su and J. R. Schrieffer, "Fractionally charged excitations in charge-density-wave systems with commensurability 3," Phys. Rev. Lett. **46**, 738–741 (1981).
42. V. M. Martinez Alvarez and M. D. Coutinho-Filho, "Edge states in trimer lattices," Phys. Rev. A **99**, 013833 (2019).
43. M. Jangjan and M. V. Hosseini, "Topological phase transition between a normal insulator and a topological metal state in a quasi-one-dimensional system," Sci. Rep. **11**, 12966 (2021).
44. R. Li and Y. Hadad, "Reduced sensitivity to disorder in a coupled-resonator waveguide with disordered coupling coefficients," Phys. Rev. A **103**, 023503 (2021).
45. S. Weimann, M. Kremer, Y. Plotnik, *et al.*, "Topologically protected bound states in photonic parity–time-symmetric crystals," Nat. Mater. **16**, 433–438 (2017).
46. W. Song, W. Sun, C. Chen, *et al.*, "Breakup and recovery of topological zero modes in finite non-Hermitian optical lattices," Phys. Rev. Lett. **123**, 165701 (2019).
47. A. Stegmaier, S. Imhof, T. Helbig, *et al.*, "Topological defect engineering and PT symmetry in non-Hermitian electrical circuits," Phys. Rev. Lett. **126**, 215302 (2021).
48. K. Takata and M. Notomi, "Photonic topological insulating phase induced solely by gain and loss," Phys. Rev. Lett. **121**, 213902 (2018).
49. X.-W. Luo and C. Zhang, "Higher-order topological corner states induced by gain and loss," Phys. Rev. Lett. **123**, 073601 (2019).
50. H. Gao, H. Xue, Q. Wang, *et al.*, "Observation of topological edge states induced solely by non-Hermiticity in an acoustic crystal," Phys. Rev. B **101**, 180303 (2020).
51. H. Xue, Q. Wang, B. Zhang, *et al.*, "Non-Hermitian Dirac cones," Phys. Rev. Lett. **124**, 236403 (2020).
52. J.-R. Li, L.-L. Zhang, W.-B. Cui, *et al.*, "Topological properties in non-Hermitian tetratomic Su-Schrieffer-Heeger lattices," Phys. Rev. Res. **4**, 023009 (2022).
53. Y.-X. Xiao, G. Ma, Z.-Q. Zhang, *et al.*, "Topological subspace-induced bound state in the continuum," Phys. Rev. Lett. **118**, 166803 (2017).
54. J. Zak, "Berry's phase for energy bands in solids," Phys. Rev. Lett. **62**, 2747–2750 (1989).
55. Z. Li, J. Wu, X. Huang, *et al.*, "Bound state in the continuum in topological inductor–capacitor circuit," Appl. Phys. Lett. **116**, 263501 (2020).
56. Z.-Q. Jiao, S. Longhi, X.-W. Wang, *et al.*, "Experimentally detecting quantized ZAK phases without chiral symmetry in photonic lattices," Phys. Rev. Lett. **127**, 147401 (2021).
57. Z. Guo, J. Jiang, H. Jiang, *et al.*, "Observation of topological bound states in a double Su-Schrieffer-Heeger chain composed of split ring resonators," Phys. Rev. Res. **3**, 013122 (2021).
58. N. Goldman, G. Juzeliūnas, P. Öhberg, *et al.*, "Light-induced gauge fields for ultracold atoms," Rep. Prog. Phys. **77**, 126401 (2014).
59. W. Nie, Z. H. Peng, F. Nori, *et al.*, "Topologically protected quantum coherence in a superatom," Phys. Rev. Lett. **124**, 023603 (2020).
60. D. M. Pozar, *Microwave Engineering* (Wiley, 2011).